Journal of Hydraulic Structures
J. Hydraul. Struct., 2024;10(4):1-25
DOI: 10.22055/jhs.2024.46764.1295

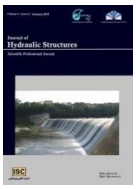

OPEN ACCESS

Comparative Assessment of the Computational Fluid Dynamics and Artificial Intelligence Methods for the Prediction of 3D Flow Field around a Single Straight Groyne

Akbar Safarzadeh [*1]
Fariborz Masoumi [1]
Zolfaghar Safarzadeh [2]
Maryam Abdoli [1]

Abstract

In this research, we investigated the three-dimensional time averaged flow pattern around a single straight groyne. To measure the three-dimensional velocity components in the laboratory, we utilized an Acoustic Doppler Velocimeter (ADV). We employed Computational Fluid Dynamics (CFD) and Artificial Neural Network (ANN) techniques to simulate the crucial flow characteristics. To validate these methods, we compared the simulation results with the measured data. The findings demonstrate that the ANN approach, with R2 values of 0.9152, 0.9150, and 0.9315, outperforms the CFD model, with R2 values of 0.8332, 0.8726, and 0.8051, in the prediction of the u and v velocity components as well as the velocity magnitude. The transverse velocity profiles indicate that the ANN method accurately predicts the velocity components and velocity magnitude, whereas the CFD method exhibits significant disparities from the measured data, particularly in the prediction of longitudinal and vertical velocity components, especially in the near-bed regions. The ANN method and the laboratory data display variations in their patterns across the shear layer and at the flow separation boundary, while the velocity profiles in the CFD method demonstrate a consistent increase from the right wall of the channel toward the main flow zone. Other flow features around the groyne, such as horseshoe vortex, secondary flow, clockwise and counterclockwise rotational flows around the groyne head and the length and precise center of the circulation zone are reasonably predicted by the ANN method. Furthermore, the ANN method accurately predicts increased velocity in the transverse direction around the groyne head and identifies two regions of amplified velocity magnitude at the cross sections downstream of the groyne in velocity magnitude contour plots. However, the values simulated by the CFD method deviate from the laboratory data.

Keywords: Groyne, Computational Fluid Dynamics, Artificial Intelligence, Horseshoe Vortex

Received: 29 April 2024; Accepted: 12 July 2024

[*] E-mail: safarzadeh@uma.ac.ir (**Corresponding Author**)
[1] Department of Civil Engineering, University of Mohaghegh Ardabili, Ardabil, Iran.
[2] Department of Civil Engineering, Ardabil branch, Islamic Azad University, Ardabil, Iran.

1. Introduction

A crucial topic in river engineering involves the erosion of river banks and its consequential impacts. This process leads to the loss of land along the riverbanks and poses a threat to nearby establishments. One primary approach to altering the river's course involves the installation of flow diversion structures, such as river groynes. Groynes, constructed from materials like riprap, gabions, or a mix of riverbed and riprap or gabion cover, are either permeable or impermeable structures. They function as a series of walls, implemented either sequentially or individually, to redirect high velocity flow away from the riverbanks. They are widely employed to safeguard outer walls in meanders, facilitate path modification, and reduce the width of the river. Furthermore, by generating low velocity circulation zones around and downstream of them, groynes promote sediment deposition near the primary shore, gradually fostering the natural development and stabilization of the riverbanks.

Despite their simple design, the construction of groynes gives rise to intricate 3D turbulent flows around them. The direct interaction of the flow with the groyne leads to the development of various vortices, giving rise to low velocity circulation zone and the formation of a wake zone in a short length upstream and a large circulation zone downstream. The presence of these phenomena, along with turbulent eddies resulting from shear layer oscillations, contributes to the complexities of the flow around the groyne.

The earliest laboratory study on groynes was carried out by Ahmad [1]. Koken & Constantinescu [2] conducted extensive research on the 3D flow structure (average and instantaneous) around a single groyne situated in a straight channel under both flat and developed bed conditions. In their study, they employed Large Eddy Simulation (LES) method for flow modeling. The researchers highlighted the significance of both local velocity amplification around the groyne head and the formation of horseshoe vortex in bed shear stress amplification.

Koken & Constantinescu [3] further examined the flow structure around a single groyne, investigating the impact of the developed bed on the formation of vortex flows and bed shear stress distribution. They concluded that the horseshoe vortex structure is more stable in a flatbed condition and significantly more complex in the instantaneous structure in the developed bed condition. Additionally, Koken & Constantinescu [4] explored the flow around a lateral obstacle using the Detached Eddy Simulation (DES) method. The primary finding of this research is the variation in the size of Separated Shear layer (SSL) vortices with changes in Reynolds number.
Duan [5] conducted a study on the average and turbulent flow structures around a straight groyne in a laboratory channel with a flat bed. In another publication by Duan et al. [6], the researchers explored the impact of a scoured hole on average and turbulent flow structures.

Koken [7] used the DES method with a Reynolds number of 45000 to study the flow around groynes with varying attachment angles (60°, 90°, 120°). The findings revealed notable variations in the size, coherence, and direction of the horseshoe vortex around the groyne.

Safarzadeh et al. [8] conducted simulations of turbulent flow in a laboratory channel and investigated the impact of altering groyne shape by using two different T-shaped groynes. The experimental findings suggest that groyne shape exerts a substantial influence on the characteristics of both average and turbulent flows, particularly in areas close to the channel bed. Safarzadeh & Brevis [9] emphasized the significance of assessing the reliability of existing numerical models for simulations and evaluated the effectiveness of Reynolds-averaged Navier-Stokes (RANS) models in predicting flow structure in a shallow open channel with a lateral obstruction. The turbulence models RSM, and were chosen for this investigation. The comparative findings revealed that the RSM model successfully predicted the length of the main

vortex area, whereas the other two models exhibited significant limitations.

Jeongsook Jeon and colleagues [10] carried out a set of laboratory investigations to analyze the flow dynamics around a rectangular groyne in an open channel. Among their key observations was the notable influence of the horseshoe vortex on the flow pattern surrounding the groyne.

Although previous studies have shown advanced performance of numerical simulations, a comprehensive numerical model still faces limitations in predicting all aspects of complex 3D flow fields due to inherent assumptions and simplifications in turbulent flow modeling. However, advanced techniques like Large Eddy Simulation (LES) and Detached Eddy Simulation (DES) have been developed, they demand high-performance computational resources for accurately calculating high Reynolds number flows, such as those around river structures. Despite extensive laboratory studies and numerical simulations, accurately simulating all flow field parameters around groynes remains a formidable challenge.

The use of soft computing methods, such as Artificial Neural Network (ANN), Genetic Programming (GP), Genetic Algorithm (GA), and others, stands in contrast to numerical simulations, offering cost-effective and intelligent solutions for complex engineering problems. These methods serve as valuable tools for addressing extensive problems that are not easily solved with traditional rule-based programs and are widely applied across various fields. AI has been employed to predict rainfall intensity [11, 12], forecast floods [13,14], estimate water quality parameters [15-17], predict the local scour depth around hydraulic structures [18-20] and determine hydraulic jump length [21-23]. Their versatility makes soft computing methods a valuable asset in addressing a wide range of water engineering challenges.

It's evident that there has been a recent focus on leveraging soft computing methods for predicting flow fields in open channels. For instance, Yang and Chang [24] assessed the effectiveness of the ANN method in simulating longitudinal velocity profiles and predicting discharge in 90° combined open channels. Additionally, Gholami, A., et al. [25] employed Computational Fluid Dynamics (CFD) and ANN methods to predict 3D flow fields in a 90° curved channel. Ebtehaj & Bonakdari [26] successfully utilized ANN to predict sediment transport in sewer pipes which is a complex phenomenon. Furthermore, Sun et al. [27] evaluated the capability of ANN models in representing and modeling flow velocity distribution of combined open-channel flow using CFD data to construct and test the ANN models. Zaji and Bonakdari [20] applied ANN and GP methods to predict longitudinal velocity field in an open channel junction, and also compared the performance of ANN, GA, and CFD methods in the same channel. Safarzadeh et al., [28] modeled the longitudinal flow field around a single straight groyne of various lengths using two computational methods, GAA and GP. The results indicated that the final chosen GAA model outperformed the final chosen GP model. Safarzadeh et al. [29] investigated the complex 3D flow field around a straight groyne using artificial neural network methods DE-MLP and DE-RBF, demonstrating the capabilities of each method in predicting certain flow field characteristics.

According to the study by Karki et al. [30], the effect of groynes orientation on near-bank flow and morphology was assessed in a natural meander bend using a two-dimensional (2D) numerical simulation. Wu and Qin [31] investigated the influence of flow and sediment transport processes on sedimentation in groyne fields with HLES model. Also, Pourshahbaz et al. [32] simulated the morphology and hydrodynamics around groynes with Flow-3D model. Pandey et al. [33] predicted the maximum scour depth near spur dikes in uniform bed sediment using stacked generalization ensemble tree-based frameworks. Ding et al. [34] investigated the flow characteristics in a mildly meandering channel with a series of groynes. In this paper, the

numerical method based on the Renormalization Group (RNG) model is used to study the effects of groynes. Xie et al. [35] employed numerical simulation to predict the 3D flow structure and turbulence characteristics near permeable spur dike in channels with varying sinuosities.

It appears that the previous studies have focused on either numerical simulations using CFD or soft computing techniques like ANN, but a comprehensive comparative evaluation of these two approaches for the groyne flow features has not been reported in the literature. The main goal of this study is to assess and compare the capabilities of CFD and ANN methods in simulating the complex time-averaged flow structures around a single straight groyne. The results obtained from both methods will be validated using measured datasets.

The details of the laboratory study are presented in the following section. Then, the two mentioned methods are introduced and the settings for each are presented. Finally, the results of each method are compared in detail.

2. Materials and Methods

2.1. Experimental Study

Figure 1 illustrates the laboratory experiments conducted in a flume with a length of 11 meters and a rectangular cross-section with a width and depth of 1 meter. The flume's walls are made of glass, while its bottom is made of Perspex, facilitating comprehensive observation of the 3D flow field from all perspectives. Water entered the tank from below the flume through a head tank containing a curved side and bed transitions. The bed transition is outfitted with three non-submerged guide vanes designed to mitigate lateral flow oscillations upon entry into the channel. Surface waves generated by the inflowing flow are mitigated by a 1.5-meter-long polystyrene plate positioned near the inlet. Additionally, an automated flap weir is installed at the downstream end of the flume to regulate the inflow depth.

The flow rate was measured using the ISOIL-MS2500 flow meter, which has an accuracy of 0.1 l.s-1. Additionally, an ultrasonic sensor with a precision of ±0.1mm was used to gauge the free water surface of the inlet. 3D velocity measurements were carried out using a 10MHz ADV instrument (Nortek, down looking type), which provides an accuracy of 0.5% and a maximum measurement frequency of 200Hz.

To position the ADV and collect data within a predefined non-uniform Cartesian grid, a fully automated traversing system with accuracies of 0.1 mm in the lateral and vertical directions, and 1 millimeter in the longitudinal direction, was utilized. The initial velocity measurements were conducted under uniform flow conditions without a groyne at different sections along the centerline of the channel, indicating full development of the flow at a distance of 8 meters from the channel inlet. In the main study, single straight groynes of different lengths (120, 150, and 200 mm) were placed in the developed section of the channel. These groynes were constructed from Perspex plates that were 1 cm thick and 20 cm high. The specific characteristics of the groynes and the hydraulic conditions of the tests are outlined in Table 1, with Uin and Hin denoting the water depth at the inlet and the bulk velocity, respectively. The inlet discharge was consistently kept at 60 l.s-1 throughout all the experiments.

According to earlier studies, changes in depth and inlet Froude number do not result in significant differences in main flow features, such as the HSV system or flow separation region. However, variations in groyne length have a noticeable effect on both average flow characteristics and turbulence characteristics [16].

The velocity measurements were carried out within non-uniform 3D grids, as shown in Figure 1, using a cartesian coordinate system (X, Y, and Z) to capture time-averaged velocity components

in the x-direction (u), y-direction (v), and z-direction (w). The measurement domain for the flow field extends to 7L upstream of the groyne and 17L downstream of it, where L represents the length of the groyne. The selection of the flow field measurement domain's extent upstream and downstream was based on the groyne's influence on near-bed flow and the recirculation zone. To capture the 3D characteristics of the flow around the tested groynes, measurements were taken on eight horizontal planes. Table 1 presents details of the measurement domains, where Zmax denotes the final horizontal measurement plane. Additionally, Nx, Ny, and Nz represent the number of measurement points in the x, y, and z directions, respectively. The sampling frequency is 100Hz, and the measurement duration at each point is 120 seconds.

The average values of the three velocity components at each measurement point were calculated and used for training and testing the neural network. Additionally, the measured data are used to validate the results of the CFD model.

Table 1: Details of the laboratory tests and geometric specifications of the tested groynes

Experiment code	Groyne length (L)	Inlet water depth (H_{in}) (mm)	$Fr=U_{in}/(gH_{in})^{0.5}$	$Re=U_{in}H_{in}/\nu$	Z_{max} (mm)	($N_x \times N_y \times N_z$)
SG-120-143	120	143	0.35	60,000	81	(20×15×8)
SG-150-143	150	143	0.35	60,000	81	(20×15×8)
SG-200-143	200	143	0.35	60,000	81	(20×15×8)

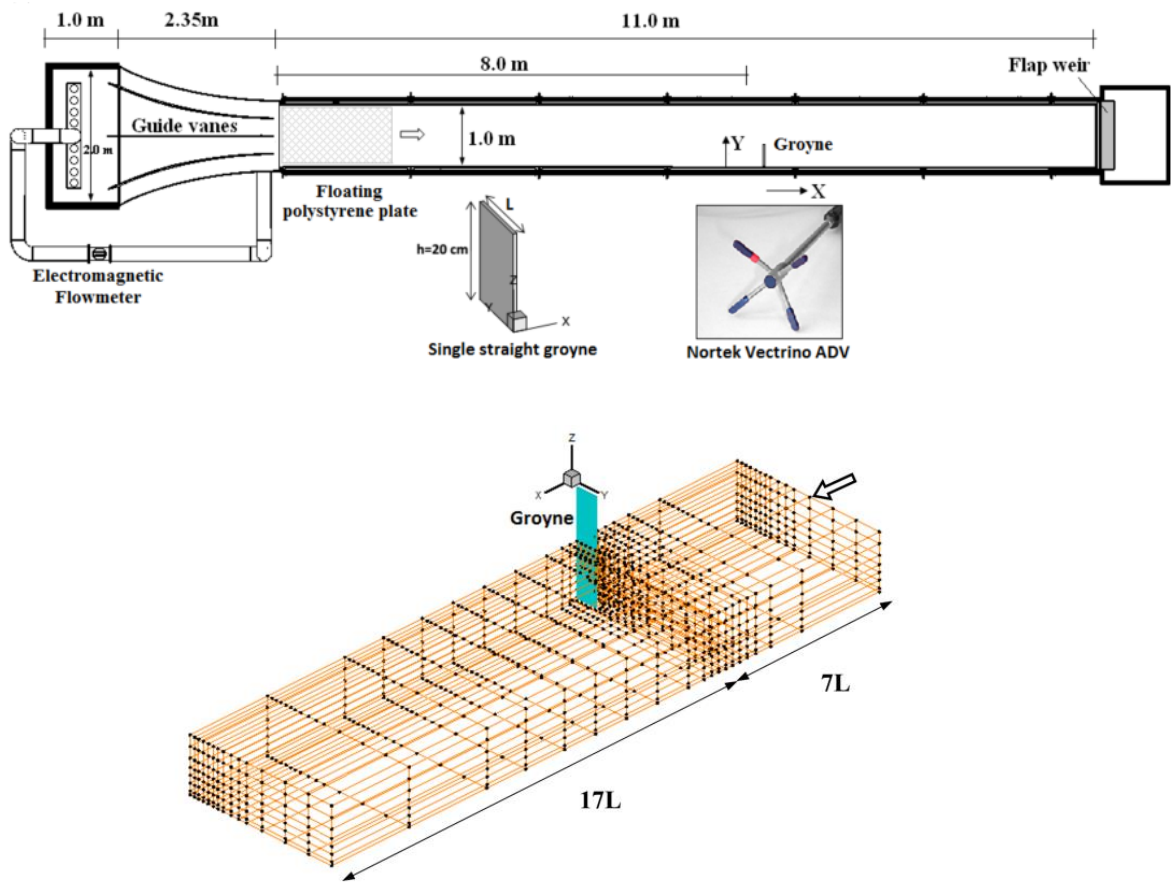

Figure 1. Laboratory flume and 3D measuring grid around a single straight groyne

The iRIC software suite was created in 2014 through a collaboration between Professor Shimizu from Hokkaido University in Japan and Dr. Nelson from the USGS Institute. The aim was to develop software for simulating river flow and morphodynamics. This extensive software includes various subprograms tailored to simulate river phenomena, such as the Nays CUBE subprogram, which was specifically designed for 3D simulation of river hydrodynamics and morphodynamics.

The fundamental equations consist of the time-averaged continuity and momentum equations, which are represented in the Cartesian coordinate system as equations 1 and 2:

$$\frac{\partial U_i}{\partial x_i} = 0 \tag{1}$$

$$\frac{\partial U_i}{\partial t} + \frac{\partial U_i U_j}{\partial x_j} = G_i - \frac{1}{\rho}\frac{\partial p}{\partial x_i} + \frac{\partial\left(-\overline{u_i u_j}\right)}{\partial x_j} + \nu\frac{\partial^2 U_j}{\partial x_j \partial x_j} \tag{2}$$

Where, $U_i$is the velocity component in the x_i Cartesian direction, ρrepresent the fluid density, $p$denotes the pressure and νcorresponds to the kinematic viscosity. On the right-hand side of the equation 2, $G_i$symbolizes the gravitational force per unit volume of the fluid. The term $-\overline{u_i u_j}$ is the Reynolds stress tensor, which is modeled in this software using the Non-linear k-ε turbulence model, as described by equation 3.

$$-\overline{u_i u_j} = \nu_t S_{ij} - \frac{2}{3}k\delta_{ij} - \frac{k}{\varepsilon}\nu_t\left[\alpha_1\left(S_{il}\Omega_{lj} + S_{jl}\Omega_{li}\right) + \alpha_2\left(S_{il}S_{lj} - \frac{1}{3}S_{km}S_{mk}S_{ij}\right)\right] + \alpha_3\left(\Omega_{il}\Omega_{lj} - \frac{1}{3}\Omega_{km}\Omega_{mk}\delta_{ij}\right)\Big] \quad (3)$$

Where, $\nu_t$denotes the eddy viscosity, k corresponds to turbulent kinetic energy and $\varepsilon$is the dissipation rate of the turbulent energy. The tensors $S_{ij}$and Ω_{ij} are the mean- rotation and mean-strain- rate tensors, respectively defined by:

$$S_{ij} = \frac{\partial U_i}{\partial x_j} + \frac{\partial U_j}{\partial x_i} \quad (4)$$

$$\Omega_{ij} = \frac{\partial U_i}{\partial x_j} - \frac{\partial U_j}{\partial x_i} \quad (5)$$

α_1, $\alpha_2$and $\alpha_3$are turbulence model parameters and they are determined based on relationships involving S and Ω, as outlined in equations 6-11.

$$\alpha_1 = -0.1325 f_M, \alpha_2 = 0.0675 f_M, \alpha_3 = -0.0675 f_M \quad (6)$$

$$f_M = (1 + m_{ds}S^2 + m_{d\Omega}\Omega^2)^{-1} \quad (7)$$

$$C_\mu = \frac{c_{\mu o}(1 + c_{ns}S^2 + c_{n\Omega}\Omega^2)}{D_\mu} \quad (8)$$

$$D_\mu = 1 + c_{ds}S^2 + c_{d\Omega}\Omega^2 + c_{ds\Omega}S\Omega + c_{ds1}S^4 + c_{d\Omega 1}\Omega^4 + c_{ds\Omega 1}S^2\Omega^2 \quad (9)$$

$$S = \frac{k}{\varepsilon}\sqrt{\frac{1}{2}S_{ij}S_{ij}} \quad (10)$$

$$\Omega = \frac{k}{\varepsilon}\sqrt{\frac{1}{2}\Omega_{ij}\Omega_{ij}} \quad (11)$$

The constant values for the above equations are provided in the software manual.

2.3. Soft Computing method

Artificial Neural Networks (ANNs), with their exceptional capability to discern patterns from complex and ambiguous data, can be utilized to uncover intricate methods that are challenging for humans and other computer techniques to comprehend. A trained neural network can be viewed as an expert in the information provided for analysis. The applications of this method in hydraulic engineering encompass predicting river floods, forecasting water quality parameters, and estimating the length of hydraulic jumps and friction coefficients in open smooth channels. The data in artificial neural networks is typically categorized into two groups: Training data, which is used to educate the network (comprising approximately 70 to 80 percent of the data), and Testing data, which serves as the primary benchmark for evaluating the proximity of predicted values to actual data (encompassing about 20 to 30 percent of the data). The steps involved in simulating artificial neural networks are as follows:

1. Collecting a sufficient set of inputs and outputs of the desired model (wherein data is generated by a numerical model, laboratory model, or real system measurements);
2. Selecting a suitable number of input-output sets as the training set, with the remainder designated as the test set. The artificial neural network model is then trained using the training set, involving the calculation of the model's parameters, i.e., weights and biases;
3. Entering the inputs of the training set into the designed artificial neural network with the parameters obtained from the previous step, and recording the calculated outputs;
4. Comparing the calculated outputs from the previous step with the real outputs, and recording the difference as the model's error;
5. Determining the calculated error for different ratios of training and test values;
6. Selecting an appropriate number of training sets by comparing the obtained values, and recording the final network parameters based on these values;
7. Continuing the algorithm by adjusting the network architecture until achieving a network with the lowest error.

During the network training process, the mean square error (MSE) between computed and observed values (as depicted in equation 12) serves as the fitness function, guiding the network training to minimize this error. In this equation, the results obtained from the artificial neural network (ANN) are denoted as "*Numerical*," while the laboratory results are represented as "*Observed*." Ultimately, a low MSE signifies high accuracy of this method.

$$MSE = \frac{\sum_{i=1}^{n}(Observed_i - Numerical_i)^2}{n} \tag{12}$$

In the above relation, n represents the number of data. The structure of artificial neural networks is presented in Figure 2, which may be single-layer or multi-layer.

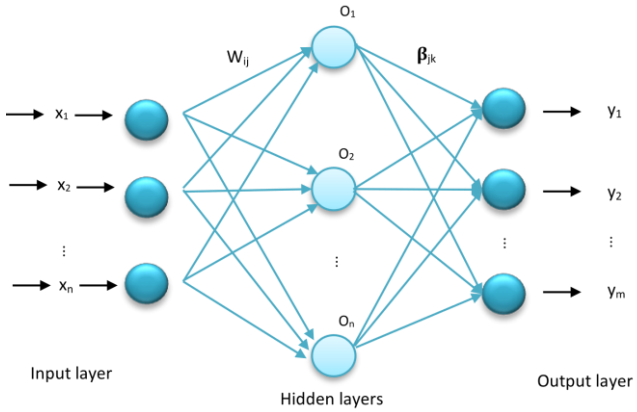

Figure 2. Structure of the MLP-ANN method.

3. Model Development

3.1. Numerical modeling in iRIC (NaysCUBE) software

A three-dimensional model was created to simulate a 11-meter-long and 1-meter-wide channel with a perpendicular groyne extending from the right channel wall into the main stream, measuring 15 cm in length and 1 cm in thickness. The groyne was treated as an obstruction. The domain was discretized using cartesian mesh. The mesh independency test, conducted using the grid convergence index (GCI) method suggested that the optimum number of grids are (450 × 50 × 15) in the x, y, and z directions, respectively [36].

A Manning coefficient of 0.01 was uniformly applied to the channel bed and side walls. At the western boundary of the computational domain (the inlet boundary), a constant discharge Q=60 $l.s^{-1}$ is imposed. The downstream boundary of the domain is defined as a constant water depth of 125 mm, which maintains the inlet water depth at 143 mm.

The model utilized the upwind numerical discretization method and employed the non-linear k-ε two-equation model for turbulence modeling. The depicted model can be seen in Figure 3, with points P_1 and P_2 serving as monitor points for overseeing the convergence of the numerical simulation.

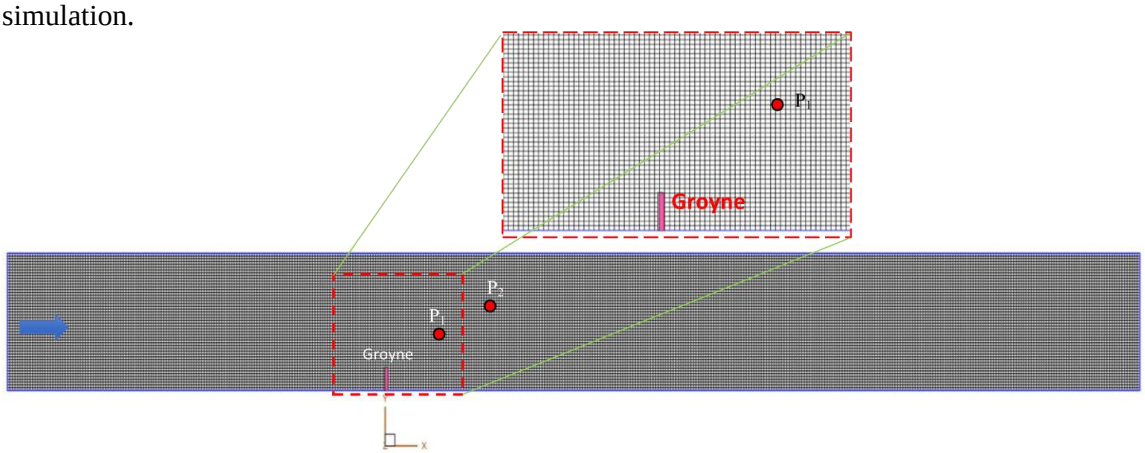

Figure 3. Computational domain in the CFD model (iRIC NaysCUBE model). Points P1 and P2 are monitor points.

3.1.1 Convergence control of numerical solution

The numerical model underwent analysis using a time step of 0.008 seconds over a duration of approximately 40 seconds. Figure 4 illustrates the temporal changes in velocity magnitude at two monitoring points, P1 and P2, situated near the channel bed and downstream of the groyne head. As shown in the figure, the solution has successfully reached complete convergence, with the velocity magnitude and other parameters stabilizing at constant values. The monitoring point locations are highlighted in Figure 3, with Point 1 positioned at X/L=1 and Y/L=2, and Point 2 at X/L=3 and Y/L=3.

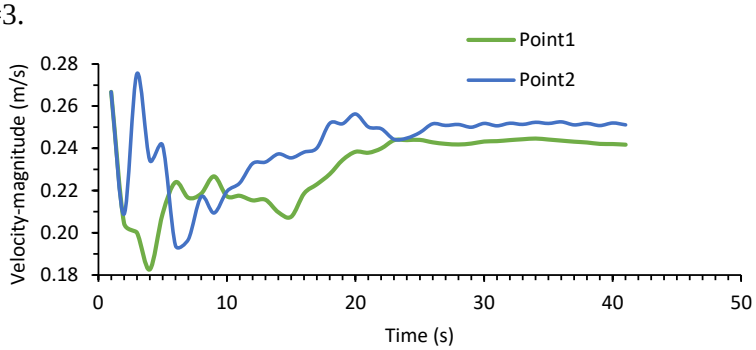

Figure 4. Numerical solution convergence for velocity-magnitude in points P1 and P2.

3.2. ANN modeling in MATLAB software

An artificial neural network was developed and trained using measured data within the MATLAB 2018b software. Following this, a testing phase was carried out using specific test numbers. The data division for testing and training was executed in the MATLAB code at a ratio of 20% for testing and 80% for training, with a random allocation process.

The input parameters in this setup included the Froude number (Fr=0.35), groyne length (L=120, 150, and 200mm), and spatial coordinates (X, Y, Z). The artificial neural network method considered the longitudinal, transverse, vertical components, and velocity magnitude (u, v, w, vel-mag) as the outputs. All input and output parameters were normalized by the groyne width (B) and input bulk velocity (Uin). Subsequently, the input parameters were dimensionless, represented as (X*=X/B, Y*=Y/B, Z*=Z/B, Fr, L/B), while the output parameters were normalized as (u*=u/Uin, v*=v/Uin, w*=w/Uin, vel-mag*=vel-mag/Uin).

For simulating the significant flow characteristics, the Multilayer Perceptron Method (MLP) was employed, featuring 24 hidden layers and 30 neurons in each layer.

4. Validation of the ANN and CFD Models

Figures 5 and 6 illustrate the comparison of the cross-sectional profiles of the three velocity components (u,v and w) and the velocity magnitude (vel-mag) in the planes close to the bed (Z=4mm) and close to the water surface (Z=81mm). A thorough examination of these figures distinctly shows the strong predictive accuracy of the Artificial Neural Network (ANN) approach for the velocity components on both planes.

The analysis of the longitudinal velocity component profile reveals a noticeable discrepancy between the simulated data from the Computational Fluid Dynamics (CFD) method and the actual measurements, particularly evident along the shear layer in both profiles compared to other regions. Specifically, the behavior of the Artificial Neural Network (ANN) method and the measured data shows fluctuations along the shear layer and at the flow separation boundary, in contrast to the consistent velocity increase from the channel's right wall towards the flow center observed in the CFD method velocity profiles.

The examination of the transverse velocity component in both profiles indicates a rise in this component near the groyne head. Assessing the velocity increase in this area is crucial for understanding local scour and groyne stability. Both forecasting approaches provide reasonably accurate results with lower values, but the precision of the Artificial Neural Network (ANN) method exceeds that of the Computational Fluid Dynamics (CFD) method. In figure 5-D, the velocity magnitude values obtained from simulations using both the ANN and CFD methods are compared with actual data near the bed. It is clear that the CFD method, which has limitations in predicting the longitudinal and transverse velocity components, also exhibits a diminished capability in this aspect compared to the ANN method.

4.1. Performance evaluation statistics

The assessment of the accuracy of the Artificial Neural Network (ANN) and Computational Fluid Dynamics (CFD) methods in predicting the flow field around a single straight groyne has been conducted utilizing statistical indices comprising five parameters: root mean squared error (RMSE), mean absolute error (MAE), absolute deviation percent (δ), standard error prediction percent (SEP), and correlation coefficient (R). The equations for these parameters are provided below:

$$RMSE = \sqrt{\frac{\sum_{i=1}^{N}(e_i - o_i)^2}{N}} \tag{13}$$

$$R = \frac{\sum_{i=1}^{n}(o_i - \bar{o})(e_i - \bar{e})}{\sqrt{\sum_{i=1}^{n}(o_i - \bar{o})^2 \sum_{i=1}^{n}(e_i - \bar{e})^2}} \tag{14}$$

$$MAE = \frac{1}{N}\sum_{i=1}^{N}|e_i - o_i| \tag{15}$$

$$\delta\% = \frac{\sum_{i=1}^{n}|(e_i - o_i)|}{\sum_{i=1}^{n} e_i} \times 100 \tag{16}$$

$$SEP\% = \frac{100}{\bar{o}} \times RMSE \tag{17}$$

In this equation, "e_i" represents the predicted data, "o_i" represents the measured data, $\bar{e}$ is the average of the predicted data, "$\bar{o}$" is the average of the measured data, and "N" is the total number of data points.

The lower values of the RMSE, MAE, δ, and SEP parameters, along with the higher values of the R parameter, indicate superior model performance. RMSE provides the standard deviation of the residuals, while MAE calculates the mean absolute residuals. These parameters offer the advantage of producing error values in the same unit as the model output, providing a reliable representation of the model's performance. Additionally, the δ and SEP methods yield dimensionless error values that are suitable for comparing cases with different scales. The R parameter indicates the linear correlation coefficient between two parameters, approaching 1 for accurate prediction and 0 for poor performance.

The quantitative assessment results of the u, v, w, and velocity-magnitude components by both methods are displayed in Table 2. Based on the data presented, the ANN method, characterized by lower RMSE values, exhibits superior predictive performance compared to the CFD method for parameters u, v, and velocity magnitude.

Table 2: Quantitative Results of Component Prediction u ،v ،w & vel-mag

Prediction Parameters	Prediction method	RMSE	MAE	δ%	SEP%	R-square
u	CFD	0.0999	0.0774	21.0200	27.1407	0.8332
	ANN	0.0664	0.0398	10.8208	18.0445	0.9152
v	CFD	0.0430	0.0337	46.0656	58.7075	0.8726
	ANN	0.0269	0.0189	25.7683	36.6755	0.9150
w	CFD	0.0152	0.0104	429.1606	630.7778	0.5985
	ANN	0.0194	0.0076	316.0246	804.3308	0.2474
vel-mag	CFD	0.0987	0.0746	18.7322	24.7845	0.8051
	ANN	0.0536	0.0390	9.7786	13.4531	0.9315

Figure 7 displays scatter plots of the parameters u, v, w, and vel-mag obtained from modeling using the ANN and CFD methods. In this representation, the measured data is depicted on the horizontal axis, while the predicted values by both methods are shown on the vertical axis. The plots reveal that the ANN method showcases a more uniformly distributed pattern of the mentioned parameters around the y=x line, indicating a heightened level of accuracy associated with this method.

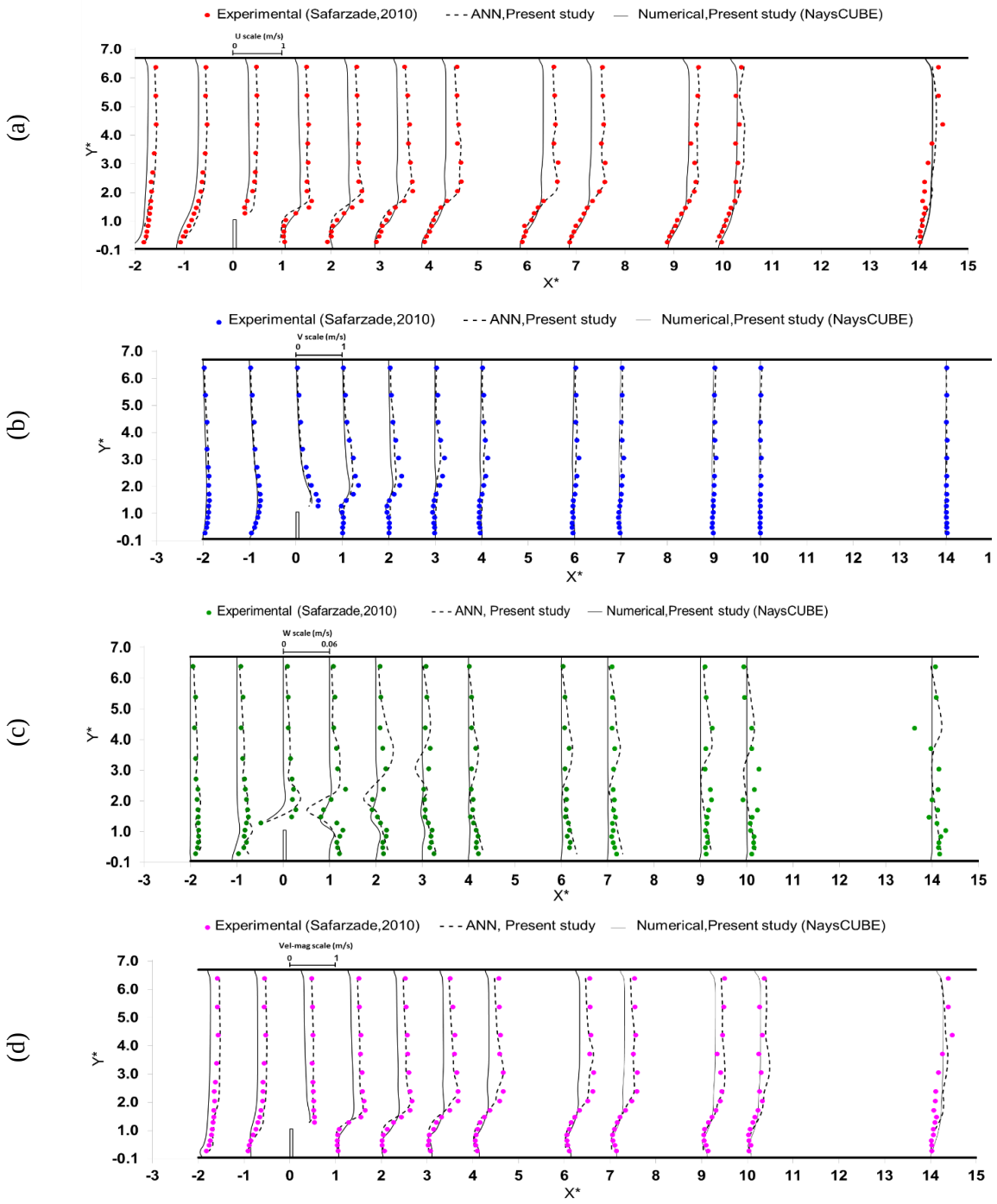

Figure 5. Comparative analysis of the experimental data, CFD modelling results, and ANN predictions in near-bed layer for different velocity components: (a) longitudinal velocity, (b) transverse velocity, (c) vertical velocity and (d) velocity magnitude.

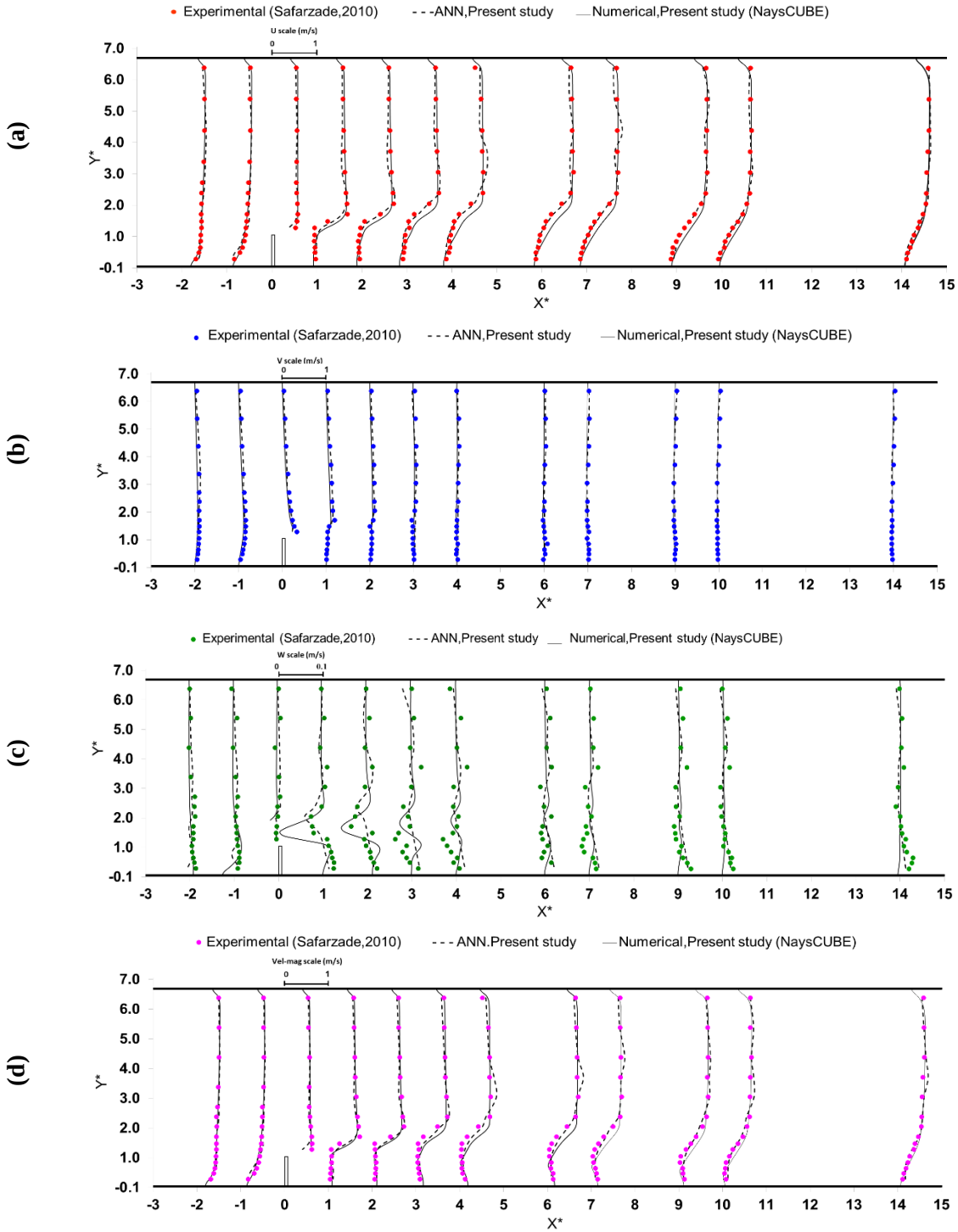

Figure 6. Comparative analysis of the experimental data, CFD modelling results, and ANN predictions in near-water surface layer for different velocity components: (a) longitudinal velocity, (b) transverse velocity, (c) vertical velocity and (d) velocity magnitude.

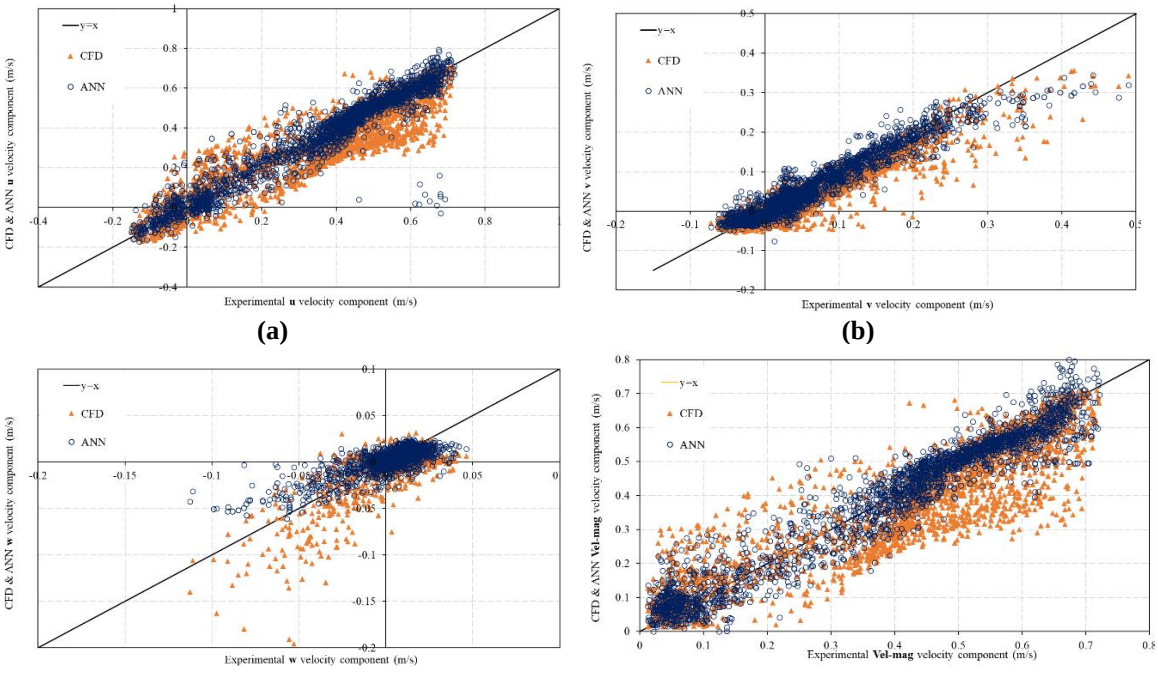

Figure 7 Comparison between the CFD and ANN study results with measured data in velocity scatter plots for different components: (a) u, (b) v, (c) w, and (d) velocity magnitude (vel-mag).

5. 2D and 3D flow features predicted by ANN and CFD methods

Figure 8 demonstrates the flow structure downstream of a single groyne, highlighting a discernible separation zone within the flow domain. While both the Artificial Neural Network (ANN) and Computational Fluid Dynamics (CFD) methodologies have offered predictions for the overall flow structure, the 3D flow pattern within the separation area, as anticipated by the ANN, closely resembles the actual experimental flow field. The streamlines depicted for the experimental flow and ANN indicate a downstream migration of the core circulation zone from the near-bed plane to the upper planes, whereas the vortex region centroids in the CFD simulation are approximately oriented vertically.

Figure 9 displays the 2D velocity vectors near the water surface. In both methods, towards the upper region of the field and distanced from the groyne structure, the vectors are notably parallel and aligned along the channel's sidewalls. As they approach the groyne, they gradually diverge and tilt towards the channel's central section. The ANN method accurately predicts the behavior of these velocity vectors, whereas the CFD method shows more deviation in the upper part of the groyne. In Figure 9a, it is evident that the length of the circulation zone is approximately 12 times the length of the groyne in the ANN prediction, while in the CFD prediction, this length reduces to around 10.2 times the groyne length, indicating a discrepancy between the measured data and CFD prediction.

In the CFD method, the center of the circulation zone is positioned closer to the groyne body than observed in the experimental results. On the other hand, the ANN method accurately forecasts the center's location. While both methods successfully predict the main flow phenomena within the field, the ANN method outperforms in modeling the precise location of these phenomena with higher accuracy.

To explore the 3D flow structure, secondary flows at different sections both upstream and downstream of the groyne are illustrated in Figure 10 (on the right side). When examining the figures in the upstream region of the groyne, primary flows exhibit a unidirectional transverse flow from the right wall of the channel to the opposite wall, a prominent pattern observed in both of the CFD and ANN methods. As the flow approaches the groyne section, the initial unidirectional transverse flows transition into rotational flows within the section, forming a clockwise secondary cell (A) in the separation zone at cross-section X/L=2. This flow pattern is clearly visible in Figure 10-b (on the right side) using the CFD method, while the ANN method also predicts this phenomenon, albeit with lower values. This flow progresses along the channel towards the water surface and eventually dissipates at cross-section X/L=14. In the CFD method, the rotational flow (A) extends to cross-section X/L=8, whereas the ANN method extends this flow up to cross-section X/L=14. Additionally, a significant upward flow emerges along the right channel wall, supported by both measured and ANN data. Remarkably, this flow characteristic was not predicted by the CFD method.

An additional rotational flow (B), characterized by a counterclockwise rotation distinct from the previously mentioned rotational flow, is observed in the relevant figure of the experimental results. As depicted in Figure 10, this type of flow has been accurately predicted by the ANN method, in contrast to the CFD method. The centers of these two rotational zones are spatially separated along the length of the field, a distinguishing feature that is clearly observable in the ANN method's predictions.

At cross-sections X/L=14 and 17, corner vortices emerge at the junction of the right channel wall and the bed, forming a rotational flow labeled as C in the experimental results. Surprisingly, this phenomenon was not anticipated by either the CFD or ANN method.

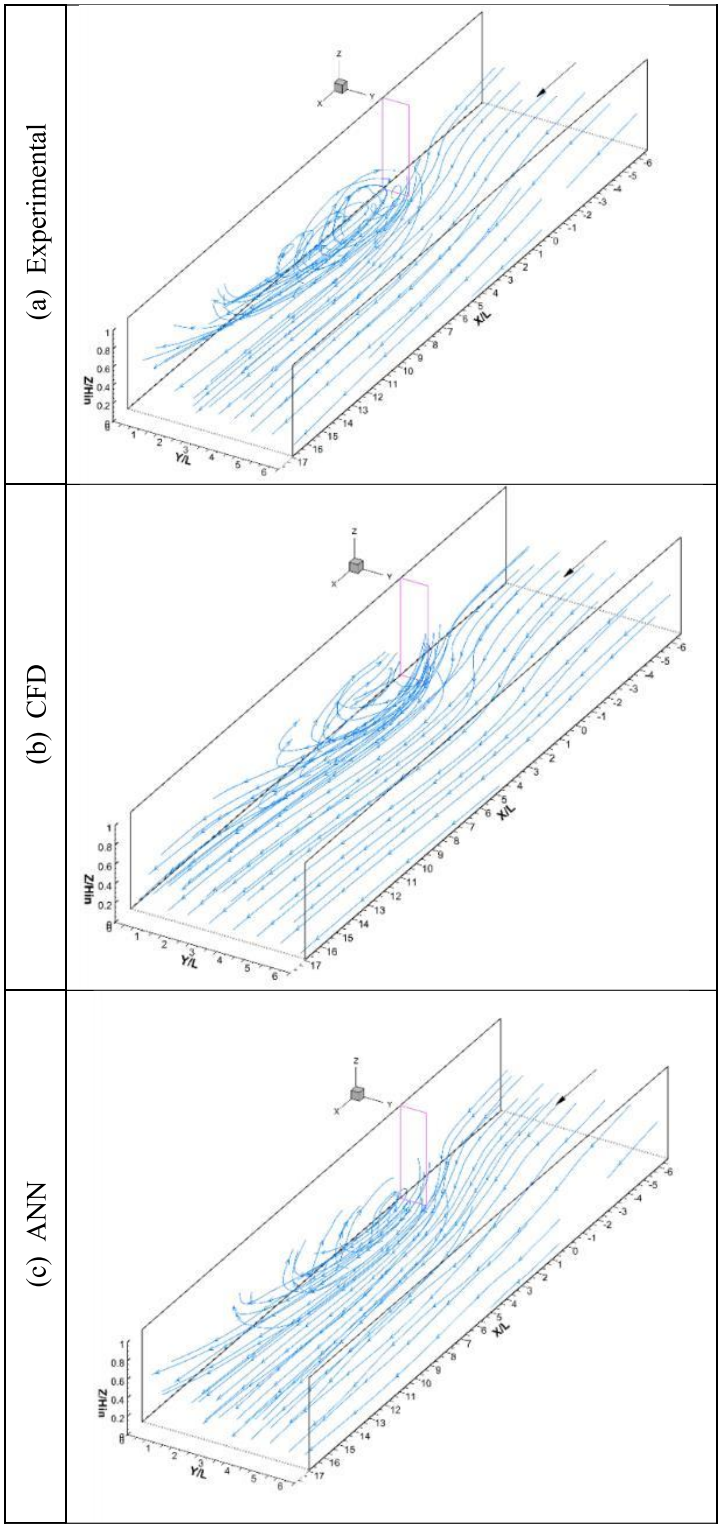

Figure 8. Visualization of 3D streamlines around a straight groyne showing: (a) Experimental results, (b) CFD simulation, and (c) ANN prediction.

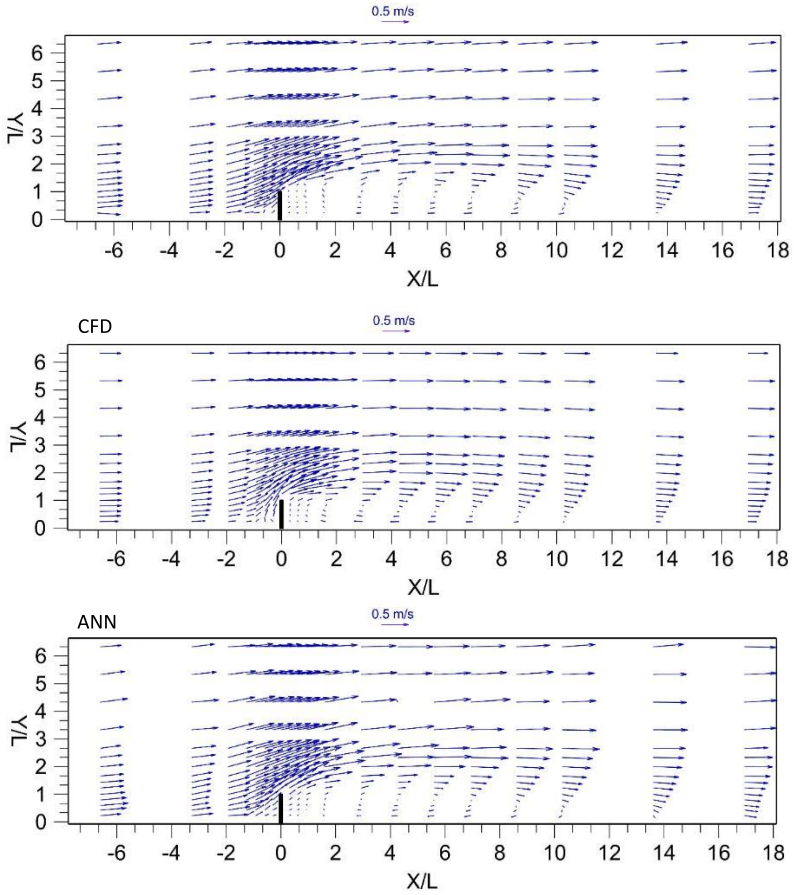

Figure 9. Representation of 2D Velocity Vectors in the plane near the water surface illustrating: (a) Experimental results, (b) CFD simulation, and (c) ANN prediction.

For a more accurate assessment of the flow field predictions made by the ANN and CFD methods, contour plots displaying the velocity magnitude distribution within different cross-sections in Figure 10 (left side) are included to facilitate an in-depth analysis.

A comparison of velocity contours between the measured data and results from both methods at cross-sections X/L=-2 and -4 indicates a consistent flow pattern with an approximate velocity of 0.42 m/s. Both the ANN and CFD methods demonstrate similarities to the experimental flow. Experimental results display an increase in velocity in the groyne section and the main flow channel, reaching around 0.55 m/s, a trend accurately captured by both methods. However, the CFD method shows slightly lower values. Beyond the groyne section, two distinct areas of intensified velocity emerge. One area corresponds to the flow core's velocity increase due to flow constriction, leading to a general velocity amplification, while the other area relates to localized velocity intensification downstream of the groyne and near the shear layer, displaying higher velocities than the previous high-velocity region. The CFD method fails to predict these two areas, although it anticipates the high-velocity region. Conversely, the ANN method does not differentiate between these two zones.

As we move downstream, the impact of the groyne gradually diminishes along the shear layer, and the heightened-velocity region gradually fades away. In the experimental results, beyond X/L=11, this region completely vanishes, giving way to a gradual velocity increase

towards the channel center up to the final section. This flow behavior has been precisely forecasted by the ANN method. The CFD method similarly illustrates this flow trend, albeit with slightly lower values.

Figure 11 displays the distribution of the vertical velocity component and secondary flow structures in cross-sections perpendicular to the horseshoe vortex's path. In Figure 11-a (experimental data), within the upstream area of the groyne head, the contours of the vertical component and velocity vectors reveal a juxtaposition of upward (positive flow) and downward vertical flows, indicating the presence of the horseshoe vortex with its peak intensity in this region. The clockwise and counterclockwise rotational zones (secondary flows) mentioned earlier are clearly visible in these sections, with their size expanding but their strength diminishing downstream, indicating the weakening of the horseshoe vortex along this trajectory. The delineated lines along the shear layer formation highlight the appearance of the horseshoe vortex in between. Both the CFD and ANN methods capture the downward vertical flow in the upstream groyne region, with varying magnitudes, the ANN method demonstrating higher accuracy. While both methods predict positive vertical component values, they do so at lower levels. The secondary flows around the groyne head are evident in both methods, but unlike the experimental findings, they wane along the trajectory.

In Figure 12 depicting streamlines at the XZ plane upstream of a single groyne (Y/L=0.3), a color contour plot of the w-velocity is included. The streamlines in the experimental figure exhibit characteristics of the near-bed Horseshoe Vortex (HSV) in the proximity of the upstream face of the groyne. The separation of the bed boundary layer and the rolling up of the incoming flow due to the reversed flow at the groyne's base are prominently highlighted. The 2D HSV forecasted by the CFD method aligns reasonably well with the observed HSV structure, but disparities exist in the location of formation and the magnitude of the HSV compared to the laboratory data. The ANN method also predicts this phenomenon with a lesser degree of approximation.

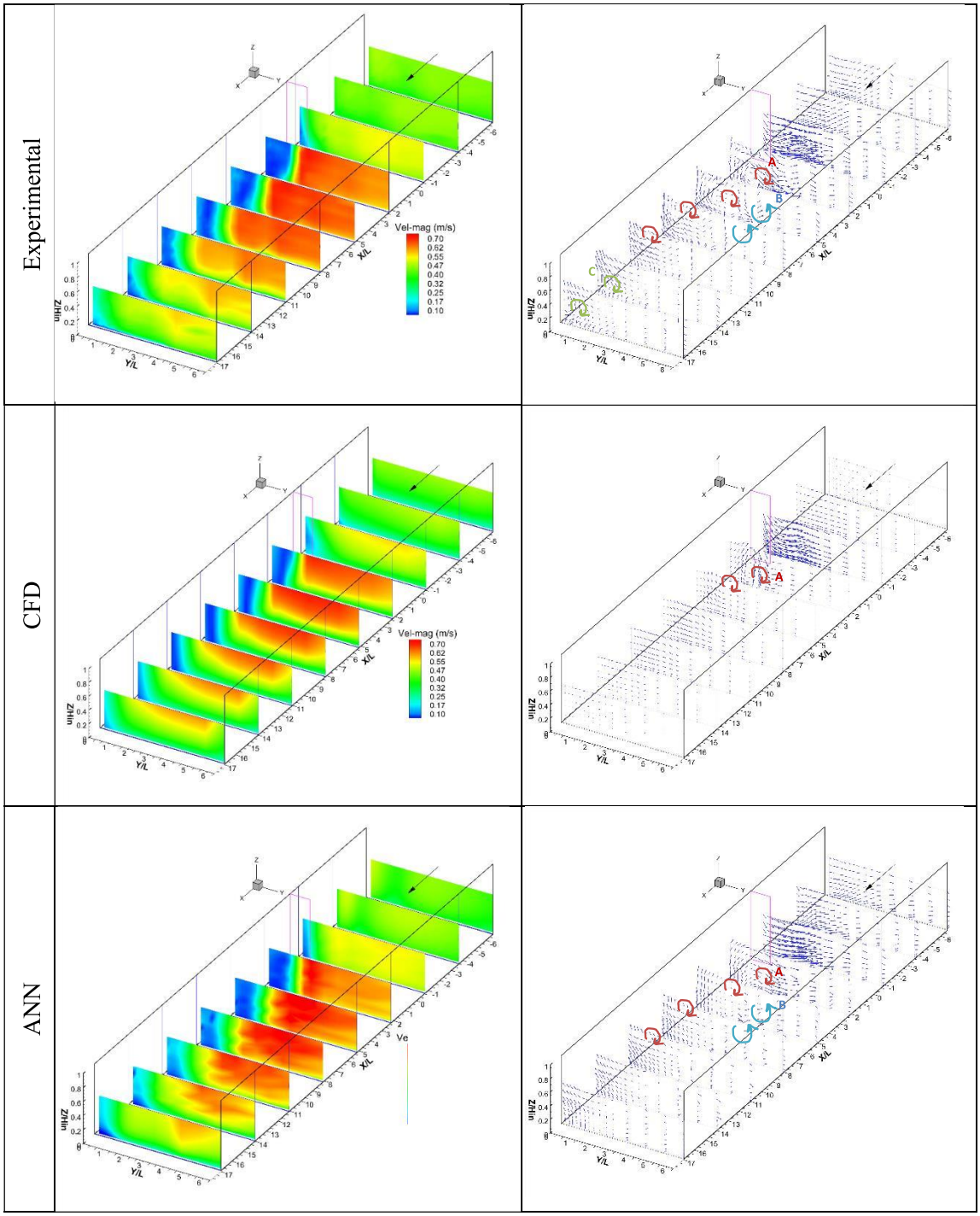

Figure 10. Comparison of the velocity magnitude and secondary flows in various cross sections around a straight groyne between experimental results, CFD simulation and ANN prediction.

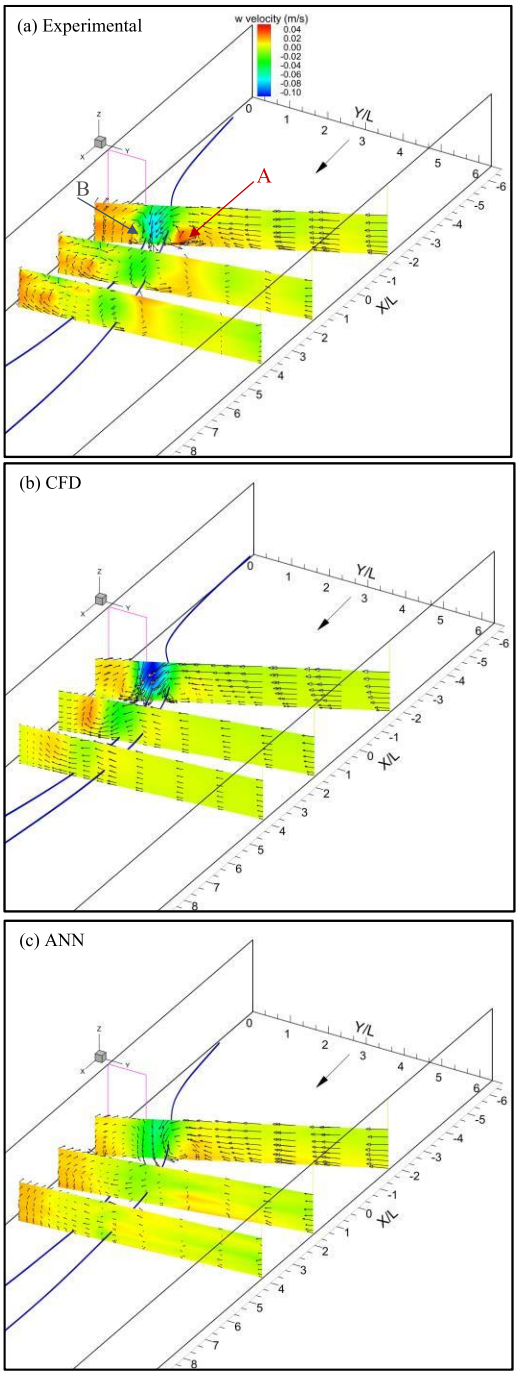

Figure 11. Comparison of the structure of the secondary flows in sections perpendicular to the horseshoe vortex path using: (a) experimental data, (b) CFD simulation, and (c) ANN prediction.

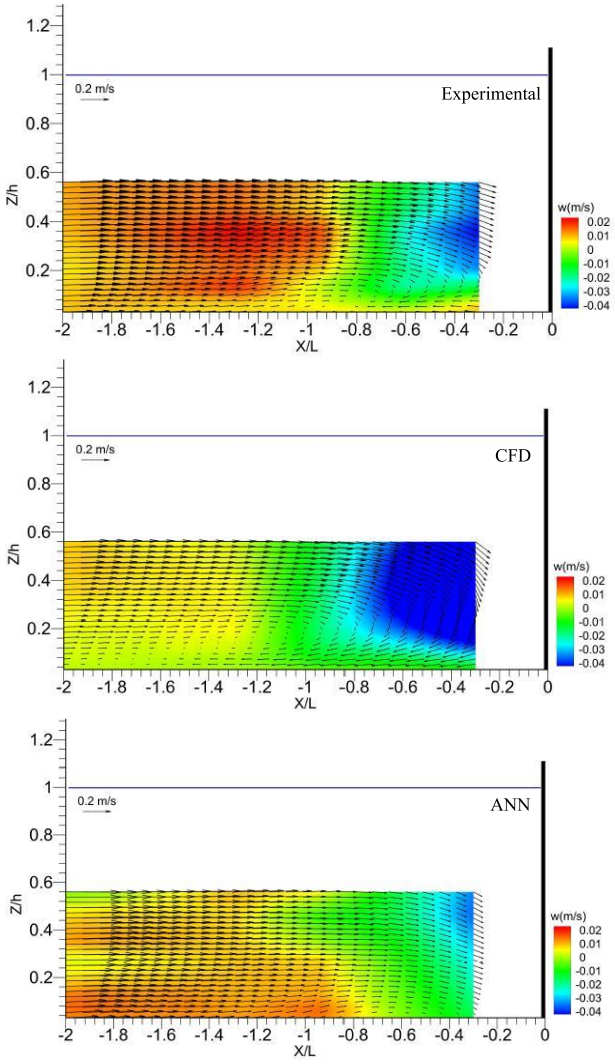

Figure 12. Comparison of the velocity vectors at Y/L=0.3 plane, upstream of the tested groyne between Experimental results, CFD simulation & ANN prediction (the contours depict the distribution of the w velocity component).

6. Conclusion

In this investigation, the 3D flow field around a single straight groyne was analyzed using Computational Fluid Dynamics (CFD) and Artificial Neural Network (ANN) methods. The ANN model incorporated dimensionless parameters X*, Y*, Z*, Froude number (Fr), and groyne length L* as inputs. The accuracy of the ANN model in predicting velocity component profiles and velocity magnitudes on near-bed and free surface planes was assessed against experimental data (Safarzadeh, 2010). The CFD analyses were conducted with the iRIC model using the nonlinear k-ε turbulence model to close the Reynolds-Averaged Navier-Stokes (RANS) equations.

The quantitative evaluation findings indicated that the ANN method excelled over the CFD method in forecasting the longitudinal (u), transverse (v), and velocity magnitude parameters,

demonstrating lower Root Mean Square Error (RMSE), Mean Absolute Error (MAE), and higher R-values. Conversely, the CFD method displayed notable discrepancies from the experimental data, especially in the near-bed zones.

The examination of transverse velocity profiles indicated that the ANN method successfully represented the changes in velocity components and magnitude across the shear layer and at the flow separation boundary. In contrast, the CFD method exhibited a consistent rise from the channel wall towards the main flow zone, deviating from the expected behavior observed in the ANN model.

Upon further analysis of streamlines and velocity vectors, it was observed that the CFD method underestimated the length of the recirculation zone, in contrast to the precise prediction made by the ANN method.

The analysis of 2D and 3D contour and velocity vector plots highlighted the ANN method's capability to reasonably predict important flow characteristics such as the horseshoe vortex around the groyne head in the lower layers, secondary flows in sections downstream of the groyne, and velocity amplification at the outer boundary of the recirculation zone. Conversely, the CFD method exhibited deficiencies in accurately representing these phenomena in certain instances.

In summary, the findings suggest that the ANN method offers a more reliable and precise forecast of the intricate 3D flow field around a single straight groyne when compared to the CFD method. This underscores the potential of data-driven approaches such as ANN in tackling complex fluid dynamics issues that present challenges for conventional numerical simulations. The outcomes of this research have the potential to enhance the comprehension and simulation of flow around river structures, with implications for river engineering and hydraulic design practices.

References

1. Ahmad, M. (1953). Experiments on design and behavior of spur-dikes. Proceeding of Minnesota International Hydraulics Convention, International Association of Hydraulic Research, Madrid, Spain.
2. Koken, M., & Constantinescu, G. (2008a). An investigation of the flow and scour mechanisms around isolated spur dikes in a shallow open channel: 1. Conditions corresponding to the initiation of the erosion and deposition process. Water Resources Research, pp: 44 (8).
3. Koken, M., & Constantinescu, G. (2008b). An investigation of the flow and scour mechanisms around isolated spur dikes in a shallow open channel: 2. Conditions corresponding to the final stages of the erosion and deposition process. Water Resources Research, pp: 44 (8).
4. Koken, M., & Constantinescu, G.(2009). An investigation of the dynamics of coherent structures in a turbulent channel flow with a vertical sidewall obstruction. Physics Of Fluids, pp: 21(8).
5. Duan, J.G. (2009). Mean flow and turbulence around a laboratory spur dike. Journal of Hydraulic Engineering, pp: 135(10): 803-811.
6. Duan, J.G., He, L., Fu, X., & Wang, Q. (2009). Mean flow and turbulence around experimental spur dike. Advances in Water Resources, pp: 32(12): 1717-1725.
7. Koken, M. (2011). Comparison of coherent structures around isolated spur dikes at various angles. Journal of Hydraulic Reaserch, pp: 49(6):736-743.

8. Safarzadeh, A., Neyshabouri, S.A.A., & Zarrati, A.R. (2016). Experimental investigation on 3D turbulent flow around straight and T-Shaped groynes in a flat bed channel. Journal of Hydraulic Engineering, pp: 142(8).
9. Safarzadeh, A., & Brevis, W.(2016). Assessment of 3D-RANS models for the simulation of topographically forced shallow flows. Journal of Hydrology and Hydromechanics, pp: 64(1): 83-90.
10. Jeon, J., Lee, J. Y., & Kang, S. (2018). Experimental investigation of three-dimensional flow structure and turbulent flow mechanisms around a nonsubmerged spur dike with a low length-to-depth ratio. Water Resources Research, pp: 54(5): 3530-3556.
11. Kan, G., Yao, C., Li, Q., Li, Z., Yu, Z., Liu, Z., Ding, L., He, X., Liang, K. (2015). Improving event-based rainfall-runoff simulation using an ensemble artificial neural network based hybrid data-driven model. Stochastic Environmental Research and Risk Assessment, 29(5):1345–1370.
12. Wu, J., Long, J., Liu, M. (2015) Evolving RBF neural networks for rainfall prediction using hybrid particle swarm optimization and genetic algorithm. Neurocomputing, 148:136–142.
13. Chaowanawatee, K., & Heednacram, A. (2012). Implementation of cuckoo search in RBF neural network for flood forecasting. Proceeding of the fourth international conference on computational intelligence, communication systems and networks, pp: 22-26.
14. Xie, JC.,Wang, TP., Zhang, JL., Shen, Y. (2010) Amethod of flood forecasting of chaotic radial basis function neural network. Proceedings of 2nd International Society of Automation, Wuhan, China.
15. Li, S., Zhao, N., Shi, Z., & Tang, F. (2010, June). Application of artificial neural network on water quality evaluation of Fuyang River in Handan city. Proceedings of International Conference on Mechanic Automation and Control Engineering, pp: 1829-1832.
16. Najah, A., El-Shafie, A., Karim, OA., El-Shafie, AH. (2013) Application of artificial neural networks for water quality prediction. Neural Computing and Application, 22(1):187–201.
17. Shen, XQ., He, TD. (2012)Water quality evaluation based on RBF neural network with parameters optimized by PSO algorithm. Proceedings of Sarvajanik College of Engineering &Technology, Wuhan University, China.
18. Bateni, SM., Borghei, SM., Jeng, DS. (2007) Neural network and neurofuzzy assessments for scour depth around bridge piers. Engineering Applications of Artificial Intelligence, 20(3):401–414.
19. Begum, SA., Fujail, AKM., Barbhuiya, AK. (2011) Radial basis function to predict scour depth around bridge abutment. Proceedings of 2nd National Conference on Emerging Trends and Applications in Computer Science, pp: 1-7.
20. Zaji, A.H., & Bonakdari, H.(2015). Application of artificial neural network and genetic programming models for estimating the longitudinal velocity field in open channel junctions. Flow Measurement and Instrumentation, Elsevier, pp: 41:81-89.
21. Abbaspour, A., Farsadizadeh, D., Ghorbani, MA. (2013) Estimation of hydraulic jump on corrugated bed using artificial neural networks and genetic programming. Journal of water scienc and engineering, 6(2):189–198.
22. Houichi, L., Dechemi, N., Heddam, S., Achour, B. (2013) An evaluation of ANN methods for estimating the lengths of hydraulic jumps in U-shaped channel. Journal of Hydroinformatics, 15(1):147–154.
23. Naseri, M., Othman, F. (2012) Determination of the length of hydraulic jumps using artificial neural networks. Advances in Engineerig Software, 48:27–31.

24. Yang, H. & Chang, F. (2005). Modelling combined open channel flow by artificial neural network. Hydrological Processes, pp: 19(18): 3747 – 3762.
25. Gholami, A., Bonakdari, H., Zaji, A., & Akhtari, A. (2015). Simulation of open channel bend characteristics using computational fluid dynamics and artificial neural networks. Engineering Applications of Computational Fluid Mechanics, pp: 9 (1): 355-369.
26. Ebtehaj, I. & Bonakdari, H. (2013). Evaluation of sediment transport in sewer using artificial neural network. Engineering Applications of Computational Fluid Mechanics, pp: 7(3): 382-392.
27. Sun, S., Yan, H., & Kouyi G. (2014). Artificial neural network modelling in simulation of complex flow at open channel junctions based on large data sets. Environmental Modelling & Software, pp: 62:178-187.
28. Safarzadeh, A., Zaji, A.H., & Bonakdari, H.(2017). Comparative assessment of the hybrid genetic algorithm–artificial neural network and genetic programming methods for the prediction of longitudinal velocity field around a single straight groyne. Applied Soft Computing, Elsevier, pp: 60: 213-228.
29. Safarzadeh, A., Zaji, A.H., & Bonakdari, H.(2018). 3D flow simulation of straight groynes using hybrid DE-based artificial intelligence methods. Springer Nature, pp: 23(11): 3757-3777.
30. Karki, S., Nakagawa, H., Kawaike, K., Hashimoto, M., & Hasegawa, Y. (2020). Assessing the effect of groynes orientation on near-bank flow and morphology in a natural meander bend using 2D numerical simulation. Proceedings of River Flow conference, Netherlands.
31. Wu, T., & Qin, J. (2020). Influence of flow and sediment transport processes on sedimentation in groyne fields. Journal of Coastal Research, 95, 304-309.
32. Pourshahbaz, H., Abbasi, S., Pandey, M., Pu, J. H., Taghvaei, P., & Tofangdar, N. (2020). Morphology and hydrodynamics numerical simulation around groynes. ISH Journal of Hydraulic Engineering, 28(1), 53–61.
33. Pandey, M., Jamei, M., Karbasi, M., Ahmadianfar, I., & Chu, X. (2021). Prediction of maximum scour depth near spur dikes in uniform bed sediment using stacked generalization ensemble tree-based frameworks. Journal of Irrigation and Drainage Engineering, 147 (11).
34. Ding, C., Li, C., Song, L., & Chen, S. (2023). Numerical investigation on flow characteristics in a mildly meandering channel with a series of groynes. Sustainability, 15(5).
35. Xie, P., Li, C., Lv, S., Zhang, F., Jing, H., Li, X., & Liu, D. (2023). Numerical simulation of 3D flow structure and turbulence characteristics near permeable spur dike in channels with varying sinuosities. Sustainability, 15(22).
36. Roache, P. J. (1994). Perspective: a method for uniform reporting of grid refinement studies. Journal of fluids engineering, pp: 116(3): 405-413.